Doppler–Range Processing for Enhanced High-Speed Moving Target Detection Using LFMCW Automotive Radar

LUZHOU XU [ID], Senior Member, IEEE
JAIME LIEN
Advanced Technology and Projects Group, Google, Mountain View, CA USA

JIAN LI [ID], Fellow, IEEE
University of Florida, Gainesville, FL USA

Range/Doppler migration and velocity ambiguity are two well-known problems encountered in high-speed moving target detection using a linear-frequency-modulated continuous-wave automotive radar. To mitigate the problems, we introduce a simple Doppler–range processing (DRP) algorithm by first performing Doppler processing via fast Fourier transform (FFT) across slow-time samples, followed by a simple interpolation step, and then range processing via FFT along Doppler migration lines over fast-time samples. The proposed DRP algorithm can achieve full range and full velocity resolutions, as well as full coherent integration gains. It attains a computational complexity comparable to that of the conventional 2-D-FFT-based range–Doppler processing approach, computationally much more efficient than existing approaches. The proposed DRP algorithm can automatically resolve the velocity ambiguity problems. We analyze its velocity ambiguity mitigation capability in relation to the radar bandwidth and the number of slow-time samples within a coherent processing interval. The effectiveness and the computational efficiency of the proposed algorithm are demonstrated by numerical examples.

I. INTRODUCTION

Environmental sensing is one of the most important capabilities required for autonomous driving [1] and advanced driver-assistance systems [2]. Unlike lidar and cameras, a radar has minimal performance degradations under various weather conditions or in dust, smoke, and other obscurants and has become an indispensable sensor for modern vehicles [3].

The linear-frequency-modulated continuous-wave (LFMCW) radar is widely used in practical automotive applications [4], [5], due to its good performance and low hardware cost. An LFMCW radar usually transmits a chirp signal periodically, with its instantaneous frequency increasing or decreasing linearly with time. At the receiver, the received signal is mixed with a replica of the transmitted waveform, followed by low-pass filtering and then digitalization via an analog-to-digital converter with a sampling rate much lower than the sweeping bandwidth of the original LFMCW probing waveform. In the literature, one refers to the sample index within a chirp period as fast time, and the chirp index as slow time. In the digital domain, range–Doppler processing (RDP) is a standard approach to form range–Doppler images of targets [6]. RDP first performs range processing via fast Fourier transform (FFT) in fast time for each period of the received signal to obtain range profiles, followed by performing Doppler processing via FFT in slow time for each range bin. From the so-obtained range–Doppler images, one can detect the objects of interest and determine their distances from the radar and their radial velocities relative to the radar [6].

The aforementioned RDP approach assumes no range migration, i.e., the target movement within a coherent processing interval (CPI) is less than a range resolution bin of $\frac{c}{2B}$, with c being the speed of propagation/light and B being the radar bandwidth, and is neglected. This assumption is valid for narrowband radars. However, to achieve high-range resolution for enhanced target detection and recognition capabilities, needed for autonomous driving, the automotive radar bandwidth has been increased significantly in recent years, from tens of megahertz to hundreds of megahertz or even several gigahertz [7]. Range migration, as a result, can no longer be neglected, especially for high-speed moving targets. For example, consider two vehicles moving in opposite directions, each at a speed of 125 km/h. Their relative speed will be up to 250 km/h. Within 50 ms, the two vehicles will move 3.5 m relative to each other, about twice the length of a motorcycle and 12 range bins of an automotive radar with a moderate radar bandwidth of 500 MHz. This causes significant range migration over slow-time samples, i.e., in the range versus slow-time domain. Consequently, the radar imaging performance of high-speed moving targets degrades significantly in terms of both range and velocity resolutions and coherent integration gain.

Many algorithms have been proposed to deal with the range/Doppler migration problem in the literature. In [8], Carlson *et al.* used the Hough transform (HT) to detect range

migration lines in the range versus slow-time domain and then integrate the energy along the lines noncoherently. The HT and its variants [8] adopt either noncoherent or hybrid coherent–noncoherent approaches. They cannot be used to achieve the full coherent integration gain, resulting in a poor target detection performance, especially when the signal-to-noise ratio is low.

Keystone formatting (KF) was proposed in [9]. KF resamples the slow-time samples for each individual instantaneous frequency (i.e., fast-time sample), such that the target Doppler shifts at various instantaneous frequencies are aligned to the one at the radar center frequency. Due to its simplicity, the KF technique has been successfully used in synthetic aperture radar [6] and ground moving target indication [10], [11] applications. In these applications, the radar pulse repetition frequency (PRF) is relatively large compared to the target Doppler shifts. This leads to small variations in the target returns from one pulse to another, and hence, simple interpolation techniques, such as the nearest neighbor (NN) or linear interpolations, can be employed. However, this algorithm is not suitable for automotive radar applications, since the Doppler shifts of automotive targets can be quite large, even larger than the PRF. The target return varies rapidly from one chirp period, i.e., pulse repetition interval (PRI) or the reciprocal of the PRF, to another, making the KF method fail to work properly. Several KF variants were proposed in [12] and [13] to deal with the Doppler foldover problem. However, all of these methods are computationally expensive and are impractical for automotive radar applications.

A novel Radon-Fourier transform (RFT) was proposed in [14]–[16] and extended to automotive radar applications in [17]. Different from the HT, the RFT utilizes the coherent integration along the range migration lines, resulting in improved integration gain. In [18] and [19], a focusing method was introduced by using the backprojection (BP) algorithm. Similar to the RFT, this method performs coherent integration in the range versus slow-time domain and can achieve the full integration gain. However, in the range versus slow-time domain, each (range, velocity) pair of a moving target is within an individual range migration line. Thus, the RFT and the focusing methods must perform brute-force integration over slow-time samples for each candidate (range, velocity) pair within the imaging area, resulting in a prohibitive computational complexity.

Another well-known problem encountered in automotive radar applications is the velocity ambiguity of high-speed targets. Typically, a forward-looking automotive radar is required to detect targets with the relative velocity ranging from −400 km/h (approaching) to 200 km/h (departing), with the corresponding Doppler frequency varying from −28.5 to 57 kHz at the operating frequency of 77 GHz. Restricted by the limited frequency sweeping rate of the chirp generation technologies, the current automotive systems can hardly produce a sufficiently high PRF (>85.5 kHz) to support unambiguous Doppler/velocity estimation [20], especially for wideband operation modes.

In the literature, one uses multiple CPIs to resolve the velocity ambiguity problems. For example, in [21], Cho proposed to transmit multiple frames with different PRFs and then use the Chinese remainder theorem [22] to resolve the ambiguity. In [23], the ambiguity was resolved through tracking targets over multiple frames. More sophisticated methods can be found in [24] and [25]. All of these methods require complicated waveform design and multiframe postprocessing, resulting in increased latency in target detection. The RFT [14] and the focusing method in [18] can be used to resolve the velocity ambiguity within a CPI, but with a prohibitive computational complexities, as discussed above.

In this article, we first show that in addition to the range migration over slow-time samples, a fast-moving target also generates a significant Doppler migration over fast-time samples (i.e., instantaneous frequencies). We then analyze their relationships and derive the coherent integration gain attainable by the conventional RDP method in the presence of range/Doppler migrations. Note that throughout this article, we consider the Doppler migration over fast-time samples (i.e., instantaneous frequencies) caused by radial velocity. We do not consider the Doppler migration over slow-time samples caused by tangential velocity or acceleration [6], [18]. We introduce a high-speed moving target imaging method, referred to as Doppler–range processing (DRP). This method first performs Doppler processing via FFT over slow-time samples, followed by a simple interpolation step and then range processing via FFT along Doppler migration lines over fast-time samples. We demonstrate both theoretically and numerically that the proposed DRP algorithm can achieve full range and full velocity resolutions, as well as full coherent integration gains, while attaining a computational complexity comparable to that of the conventional RDP approach. DRP is computationally much more efficient than the existing RFT [14] and focusing [18] methods. We further prove that the proposed DRP algorithm can automatically resolve the velocity ambiguity problem, and we analyze its velocity ambiguity mitigation capability in relation to the radar bandwidth and the number of chirps, i.e., slow-time samples, within a CPI.

The main contributions of this article are summarized as follows:

1) First, this article provides new insights into the range migration problem of high-speed moving targets. We show that a fast-moving target also generates a significant Doppler variation over fast-time samples (i.e., instantaneous frequencies), in addition to the well-known range migration over slow-time samples. By compensating out this Doppler variation in the fast-time versus Doppler domain, we can solve the range migration problem more efficiently.

2) Second, we introduce a novel DRP method to mitigate the range and Doppler migration problems. DRP can achieve full range and full velocity resolutions, as well as full coherent integration gains. In

contrast to the existing RFT [14] and the focusing method in [18], DRP, with an additional simple interpolation step, takes full advantages of the FFT for both Doppler and Range processing. It attains a computational complexity comparable to that of the conventional 2-D-FFT-based RDP approach. DRP is computationally much more efficient than the existing methods in [14] and [18].

3) Third, we derive the coherent integration gains of the conventional RDP method in the presence of range/Doppler migration. We show that the integration gain of RDP decreases 3 dB per doubling of the CPI and 6 dB per doubling of the radar bandwidth or target velocity.

4) Finally, we theoretically investigate the velocity ambiguity resolving capability of the proposed DRP approach in relation to the radar bandwidth and the number of chirps, i.e., slow-time samples, within a CPI.

The rest of this article is organized as follows. In Section II, the moving target data model is established. In Section III, we discuss the range and Doppler migrations and their relationships, and also derive the RDP integration gain in the presence of range and Doppler migrations. In Section IV, we introduce the DRP method and investigate the DRP performance for high-speed target imaging. Several numerical examples are presented in Section V. Finally, Section VI concludes this article.

II. SYSTEM AND DATA MODEL

We consider an LFMCW radar and a target at a distance or range r from the radar. After dechirping and digitization, the target return can be modeled as follows [4], [5]:

$$x[n] = \beta e^{-j4\pi \frac{r(f_0 + n\gamma)}{c}} \tag{1}$$

where $n = -\frac{N}{2}, -\frac{N}{2} + 1, \ldots, \frac{N}{2} - 1$ denotes the fast-time sample index, with N being the number of samples per chirp period or PRI, which is the time interval between two adjacent chirps. For notational simplicity, we assume N to be an even number. In (1), β represents the signal complex amplitude, with its modulus proportional to the square root of the radar cross section, and f_0 and γ denote the center frequency and the instantaneous frequency increment/decrement per fast-time sample, respectively. Note that γ can be positive or negative for up- and down-chirps, respectively, and we can easily obtain the radar bandwidth as $B = N|\gamma|$.

Now, we assume that L periods of chirps are transmitted within a CPI, with L being an even number for notational convenience. Let $l = -\frac{L}{2}, -\frac{L}{2} + 1, \ldots, \frac{L}{2} - 1$ be the slow-time sample index, i.e., the chirp index. Consider a target at a distance r_0 at $l = 0$ moving with a radial velocity v. Ignoring the target movement within a chirp period or PRI, the target distance at the lth slow-time sample will be

$$r_l = r_0 + lvT_{\text{PRI}} \tag{2}$$

with T_{PRI} denoting the PRI. From (1) and (2), the received samples can be modeled as

$$x[n, l] = \beta e^{-j4\pi \frac{nr_0\gamma + lvf_0 T_{\text{PRI}} + nlv\gamma T_{\text{PRI}}}{c}} + z[n, l] \tag{3}$$

where n and l denote the fast-time and slow-time sample indices, respectively, and $z[n, l]$ contains the noise, clutter, and jamming interference. In (3), the constant phase term $e^{-j4\pi \frac{f_0 r_0}{c}}$ has been absorbed into the unknown complex amplitude β for notational simplicity.

Let $T_{\text{CPI}} = LT_{\text{PRI}}$ denote the CPI. We remark that when $\frac{2vBT_{\text{CPI}}}{c} \ll 1$, the fast- and slow-time coupling term in (3), i.e., $e^{-j4\pi \frac{nlv\gamma T_{\text{PRI}}}{c}}$, can be neglected. Then, (3) is reduced to the standard LFMCW data model after dechirping and sampling [6]. The 2-D FFT (usually with windowing to reduce sidelobe levels and zero-padding to obtain range–Doppler (RD) images on a find grid) can be applied to $x[n, l]$ for estimating β for various range and velocity pairs. This is the conventional RDP method to form RD images.

However, as discussed in Section I, in automotive radar applications, the assumption that $\frac{2BT_{\text{CPI}}v}{c} \ll 1$ may not hold, resulting in the fast- and slow-time coupling term in (3) nonnegligible. We show in Section III that this term produces range migration over slow-time samples and Doppler migration over fast-time samples. Ignoring this term can severely degrade the range and Doppler resolutions, as well as the coherent integration gains, of the resulting RD images.

III. PROBLEM IDENTIFICATION

A. Range and Doppler Migrations

In this subsection, we discuss the range migration over slow-time samples, Doppler migration over fast-time samples, and their relationships for fast moving targets with high radial velocities. Note that herein we consider the Doppler migration over fast-time samples (i.e., instantaneous frequencies) caused by radial velocity. We do not consider the Doppler migration over slow-time samples caused by tangential velocity or acceleration [6], [18].

First, applying the windowed Fourier transform to (3), with respect to n, yields the range versus slow-time image as follows:

$$X_{\text{R}}[r, l] = \sum_{n=-\frac{N}{2}}^{\frac{N}{2}-1} w_{\text{R}}[n] x[n, l] e^{j4\pi \frac{nr\gamma}{c}}$$

$$\approx \beta e^{-j4\pi \frac{lvf_0 T_{\text{PRI}}}{c}} S_R[r - r_0 - lvT_{\text{PRI}}] \tag{4}$$

where

$$S_R[r] = \sum_{n=-\frac{N}{2}}^{\frac{N}{2}-1} w_{\text{R}}[n] e^{j4\pi \frac{n\gamma r}{c}} \tag{5}$$

with $w_{\text{R}}[n]$ denoting the windowing function [6] used for range compression to reduce sidelobe levels. In (4), $S_R[r]$ behaves like a delta function roughly. Thus, the dominant reflected energy of a moving target distributes along
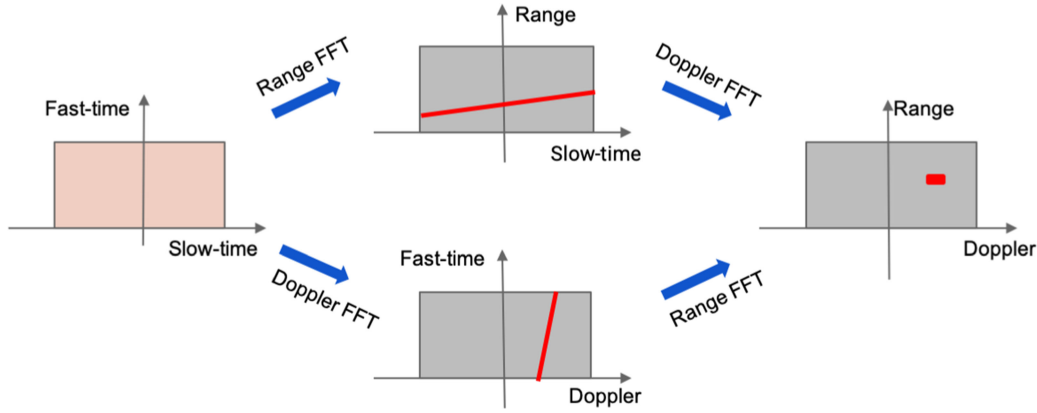
Fig. 1. Range and Doppler migrations and their relationships.

the range migration line $r = r_0 + lvT_{PRI}$ in the range versus slow-time domain (see Fig. 1). This feature is utilized by the RFT method in [14] to mitigate the range migration.

Similarly, applying the Fourier transform to (3), with respect to l, yields the fast-time versus Doppler image as follows:

$$X_D[n, f_d] = \sum_{l=-\frac{L}{2}}^{\frac{L}{2}-1} w_D[l] x[n, l] e^{-j2\pi l f_d T_{PRI}}$$

$$\approx \beta e^{-j4\pi \frac{n r_0 \gamma}{c}} S_D \left[f_d + \frac{2(f_0 + n\gamma)v}{c} \right] \quad (6)$$

where

$$S_D[f_d] = \sum_{l=-\frac{L}{2}}^{\frac{L}{2}-1} w_D[l] e^{-j2\pi l f_d T_{PRI}}. \quad (7)$$

Again, $S_D[f_d]$ can be approximated as a delta function. Thus, the dominant reflected energy of the moving target distributes along the Doppler migration line $f_d = -\frac{2(f_0+n\gamma)v}{c}$ in the fast-time versus Doppler domain (see Fig. 1).

Fig. 1 illustrates the range and Doppler migrations of a high-speed moving target and their relationships. As we can see, the range migration occurs in the range versus slow-time domain when the target moves more than one range resolution bin within a CPI, while the Doppler migration occurs in the fast-time versus Doppler domain when the Doppler variation over the fast-time samples, i.e., the instantaneous frequencies of the LFMCW radar, is larger than a Doppler resolution bin. Using the facts that the range resolution is $\frac{c}{2B}$ and the target moves vT_{CPI} within a CPI, we can readily obtain the following range migration condition:

$$\alpha \triangleq \frac{2BT_{CPI}v}{c} > 1. \quad (8)$$

The same condition in (8) can be obtained for Doppler migration, by using the facts that the Doppler resolution is $\frac{1}{T_{CPI}}$ and the Doppler variation at the minimum and maximum

instantaneous frequencies is $\frac{2Bv}{c}$. We remark that α in (8) roughly represents the number range resolution bins that the target moves within a CPI in the range versus slow-time domain, or the number of Doppler resolution bins that the target occupies in the fast-time versus Doppler domain.

We also notice that a range migration line in the range versus slow-time domain is determined by two unknown parameters, i.e., the center range r_0 and the velocity v of the target. In other words, each (range, velocity) pair corresponds to an individual range migration line. Thus, the RFT [14] and focusing [18] methods, which perform coherent integration along range migration lines, must perform brute-force integration for each (range, velocity) pair in the imaging area of interest, resulting in a prohibitive computational complexity. In contrast, from (6), we can see that the Doppler migration line in the fast-time versus Doppler domain is determined only by the velocity v of the target. In other words, targets with the same velocity at different ranges share the same Doppler migration line. This makes it possible to perform the 1-D FFT along Doppler migration lines for range processing. Based on this, we will introduce a new DRP method in Section IV to deal with the range/Doppler migration problem, which is computationally much more efficient than the existing RFT [14] and focusing [18] methods.

B. Integration Gain of RDP

RDP is a standard approach to form RD images using the LFMCW radar. It is well known that this method suffers from the range/Doppler migration problems, resulting in reduced coherent integration gain [9], [14], [18]. However, to the best of our knowledge, the integration gain in the presence of range and Doppler migrations has not been analyzed quantitatively.

In Appendix A, we show that for a large α defined in (8) and using rectangular windows for range and Doppler processing, the RDP integration gain can be approximated as

$$g_{RDP} \approx \frac{NL}{\alpha^2} = \frac{Nc^2}{4LB^2 v^2 T_{PRI}^2}. \quad (9)$$

In (9), the numerator NL represents the best achievable co-herent integration gain, while the denominator α^2 represents the gain reduction caused by the range/Doppler migrations. We can see from (9) that in the presence of range/Doppler migrations, the coherent integration gain decreases 3 dB per doubling of the number of chirps or slow-time samples L within the CPI and decreases 6 dB per doubling of the radar bandwidth B (i.e., the chirp rate γ) or the target radial velocity v.

IV. DOPPLER–RANGE PROCESSING

In this section, we first present a simple DRP method to mitigate the range/Doppler migration problem and then theoretically analyze its performance, in terms of range and velocity resolutions, coherent integration gain, and computational complexity, as well as its velocity ambiguity mitigation capability. Note that the proposed DRP method is equivalent to the RFT [14] and focusing [18] methods in performance, but with a much lower computational complexity. Thus, the theoretical analysis presented in this section, except for the computational complexity analysis, can also be applied to the methods in [14] and [18].

A. Algorithm Description

From (3), the complex-valued target amplitude β for various range–velocity pairs can be estimated via the BP principle, as follows:

$$\beta_{DRP}[r, v] = \sum_{l=-\frac{L}{2}}^{\frac{L}{2}-1} \sum_{n=-\frac{N}{2}}^{\frac{N}{2}-1} w_D[l]\, w_R[n]\, x[n,l] e^{j4\pi \frac{n r_0 \gamma}{c}}$$
$$\times\, e^{j4\pi \frac{l v f_0 T_{PRI}}{c}} e^{j4\pi \frac{n l v \gamma T_{PRI}}{c}}. \tag{10}$$

Exchanging the summation order, and after some simple manipulations, we get

$$\beta_{DRP}[r_0, v] = \sum_{n=-\frac{N}{2}}^{\frac{N}{2}-1} w_R[n] X_D\left[n, f_d(n,v)\right] e^{j4\pi \frac{n r_0 \gamma}{c}}$$
$$= \text{IFFT}_n \left\{ w_R[n] X_D\left[n, f_d(n,v)\right] \right\} \left(\frac{2\gamma r_0}{c} \right) \tag{11}$$

where

$$X_D[n, \omega] = \sum_{l=-\frac{L}{2}}^{\frac{L}{2}-1} w_D[l] x[n,l]\, e^{-j2\pi l \omega T_{PRI}}$$
$$= \text{FFT}_l \{ w_D[l] x[n,l] \}(\omega T_{PRI}) \tag{12}$$

and

$$f_d(n,v) = \left[-\frac{2(f_0 + n\gamma)v}{c} \right]_{PRF} \tag{13}$$

and $\text{FFT}_l\{\cdot\}$ and $\text{IFFT}_n\{\cdot\}$ denote FFT and IFFT operations with respect to l and n, respectively. In (12), $X_D[\cdot, \cdot]$ denotes the fast-time versus Doppler image, which can be obtained efficiently by performing Doppler processing via applying FFT to slow-time samples within the CPI for each fast-time

TABLE I
Proposed Doppler–Range Processing

I. Doppler FFT: For $n = -\frac{N}{2}, -\frac{N}{2}+1, \cdots, \frac{N}{2}-1$ Compute $X_D[n, \omega]$ by applying windowed FFT   to $x[n,l]$ with zero-padding w.r.t. l.
II. Range FFT: For each candidate v **a.** Compute $X_D[n, f_d(n,v)]$ from $X_D[n, \omega]$ via NN or linear interpolation.   **b.** Apply windowed FFT to $X_D[n, f_d(n,v)]$ with zero-padding w.r.t. n.

sample, $f_d(n,v)$ denotes the folded Doppler frequency at the nth fast-time sample (i.e., at the corresponding radar instantaneous frequency of $f_0 + n\gamma$) for a target with a true radial velocity v, and $[\cdot]_{PRF}$ denotes folding the true Doppler frequency to $[-0.5 f_{PRF}, 0.5 f_{PRF})$.

Given v, $X_D[n, f_d(n,v)]$ represents the 1-D data along the Doppler migration line in (13). Note that different from the range migration line, each Doppler migration line is determined by only one unknown target parameter, i.e., v, and is independent of r_0. Thus, $\beta_{RDP}[r, v]$ for all possible values of r_0 in (11) can be computed efficiently by applying the 1-D FFT to $X_D[n, \omega]$ along the Doppler migration lines.

Fig. 2 illustrates the DRP algorithm, with the corresponding pseudocode shown in Table I. Note that different from the conventional RDP method, the DRP algorithm performs the slow-time FFT first for Doppler processing, followed by a simple interpolation step, and then the FFT along the Doppler migration lines for range processing. Compared to the conventional RDP method, DRP needs only the extra simple interpolation step, i.e., velocity bin interpolation in Fig. 2 or Step II.a in Table I, along the Doppler migration lines. In practice, windowing the slow-time samples and then zero-padding are recommended before the FFT in Step I to obtain fine Doppler bins with low sidelobes. Then, the simple NN or linear interpolation method can be utilized in Step II.a, with a computational complexity on the order of $O(NL)$. Note also that in Step II, the scanning velocity v can be much larger than $[-0.5 V_{Ambi}, 0.5 V_{Ambi})$, resulting in a range versus velocity image much wider than its RDP counterpart. This can help mitigate the velocity ambiguity problem, as we will show in Section IV-C.

B. Range and Velocity Resolutions, Coherent Integration Gain, and Computational Complexity

Obviously, DRP attains the full coherent integration gain (see [14] and [18]). For rectangular windows, we have

$$g_{DRP} = NL. \tag{14}$$

We further prove (see Appendix B) that the DRP algorithm provides exactly the same range profile and approximately the same main-lobe shape of the velocity profiles, as for the stationary target case. Therefore, the proposed DRP algorithm can attain the full range and full
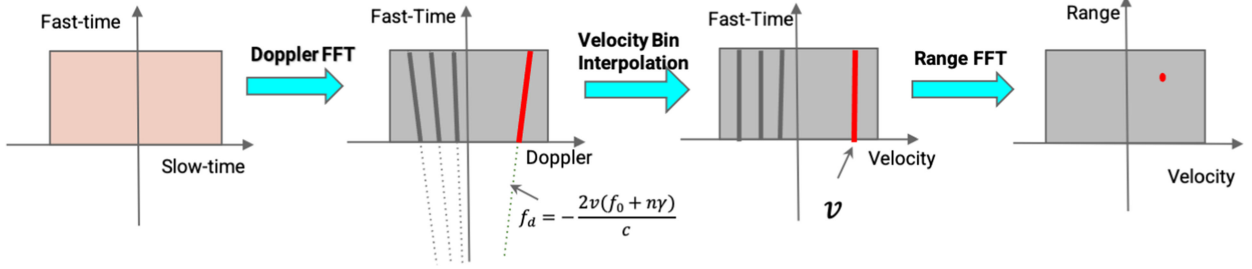
Fig. 2. Proposed DRP.

TABLE II
Computational Complexities of
Various Algorithms

Algorithm	Complexity
RDP	$O(NL\log(NL))$
KF	$O(NL\log(NL) + NL)$
RFT	$O(NL\log N + NL^2)$
DRP	$\mathbf{O(NL\log(NL) + NL)}$

velocity resolutions, i.e.,

$$\Delta_{R,\text{DRP}} = \frac{c}{2B} \quad \text{and} \quad \Delta_{V,\text{DRP}} = \frac{c}{2T_{\text{CPI}}f_0} \qquad (15)$$

respectively, for rectangular windows.

We remark that different from the RFT and focusing methods in [14] and [18], the proposed DRP algorithm can use the FFT for both the Doppler and range processing and, hence, has a much lower computational complexity than the existing methods. Compared to the conventional RDP method, DRP needs only an extra step of simple interpolations. The overall computational complexity of the DRP algorithm is on the order of $O(NL\log(NL) + NL)$, which is comparable to that of the standard 2-D-FFT-based RDP. Table II compares the computational complexities of the various algorithms discussed herein. Note that the focusing method in [18] is equivalent to the RFT [14] in both performance and computational complexity, and its computational complexity is not listed separately. From Table II, we can see that the proposed DRP method has around $\frac{L}{\log L}$ times less computational complexity than that of the RFT. In other words, DRP is 100 times more efficient than the RFT when $L = 1024$.

C. Velocity Ambiguity Mitigation

In the section, we discuss how to mitigate the velocity ambiguity using the proposed DRP algorithm.

Consider two velocity possibilities, v and $v + kV_{\text{Ambi}}$ for an integer k, of a target, with

$$V_{\text{Ambi}} = \frac{c}{2T_{\text{PRT}}f_0} \qquad (16)$$

which denotes the unambiguous upper bound of the relative radial velocity for the conventional RDP approach. The

corresponding center Doppler frequencies for the two velocities are $-\frac{2f_0 v}{c}$ and $-\frac{2f_0(v+kV_{\text{Ambi}})}{c} = -\frac{2f_0 v}{c} - kf_{\text{PRI}}$. Obviously, the conventional RDP method cannot identify the true target velocity from these two possibilities.

From (13), we can obtain the Doppler migration line for the radial velocity $v + kV_{\text{Ambi}}$ as follows:

$$\begin{aligned}
f_d(n, v + kV_{\text{Ambi}}) &= \left[-\frac{2(v + kV_{\text{Ambi}})(f_0 + n\gamma)}{c} \right]_{\text{PRF}} \\
&= \left[-\frac{2v(f_0 + n\gamma)}{c} - \frac{kn\gamma}{f_0}f_{\text{PRF}} \right]_{\text{PRF}}.
\end{aligned} \qquad (17)$$

Comparing (17) from (13), we can see that the Doppler migration lines for v and $v + kV_{\text{Ambi}}$ are different because they have different slopes with respect to n. In other words, the two Doppler frequencies are not identically the same over all the fast-time samples, i.e., across the entire radar bandwidth. Performing FFTs along these two migration lines produces different outputs. Because of the slope difference, DRP generates a stronger response at the true target velocity than at its folded counterpart. Thus, the true target velocity can be identified using DRP as the one corresponding to the stronger response. A simple example of using DRP for velocity ambiguity mitigation is shown in Fig. 3. For this example, v is positive and the other velocity possibility, $v - V_{\text{Ambi}}$, is negative. In other words, the target may move away from or approach the radar. The two Doppler migration lines are $f_d(n, v) = -\frac{2v(f_0+n\gamma)}{c}$ and $f_d(n, v - V_{\text{Ambi}}) = -\frac{2(v-V_{\text{Ambi}})(f_0+n\gamma)}{c} - f_{\text{PRF}}$, respectively.

From (3), we can readily obtain the cross-correlation coefficient of the reflected signals of two targets at the same range bin with the radial velocities being v and $v + kV_{\text{Ambi}}$, respectively, as follows:

$$\rho = \frac{1}{NL} \sum_{l=-\frac{L}{2}}^{\frac{L}{2}-1} \sum_{n=-\frac{N}{2}}^{\frac{N}{2}-1} e^{-j2\pi \frac{ln k\gamma}{f_0}}. \qquad (18)$$

When $\frac{kLB}{f_0} \gg 1$, we have (see Appendix C)

$$\rho \approx \frac{f_0}{kLB}. \qquad (19)$$

From (19), we can see that the two targets' returns become less correlated when we have a larger number of slow-time samples (i.e., the number of chirps) within a CPI or a wider radar bandwidth, which results in weaker shadows at
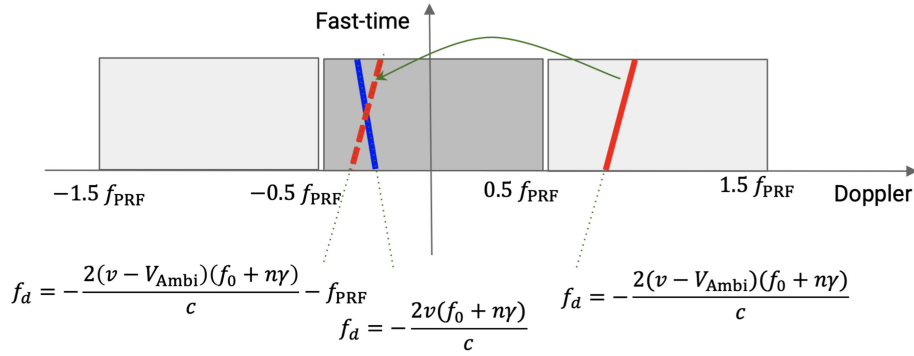
Fig. 3.   Example of velocity ambiguity mitigation using DRP.

f_0	B	T_{PRI}	N	L	r_0	v
79 GHz	500 MHz	32 μs	1024	1024	200 m	-250 km/h

the folded velocities. Intuitively, a wider radar bandwidth makes the Doppler migration lines in Fig. 3 longer, while more chirps make them thinner. Both reduce the similarity of the two Doppler migration lines, making it easier to identify the true target from its shadows.

In practice, the DRP algorithm given in Table I can be used to form a range versus velocity image, with a much wider range of potentially possible velocities than V_{Ambi}. A constant false alarm rate [6] detector can be applied to the so-formed range versus velocity image to detect potential targets. The detected targets at the same range bin but with folded velocities can be identified and discarded, while retaining the one with the largest amplitude estimate.

V.   NUMERICAL EXAMPLES

In this section, several numerical examples are provided to demonstrate the effectiveness and efficiency of the proposed DRP algorithm for high-speed moving target imaging using the LFMCW automotive radar.

In the following, we compare the proposed DRP algorithm with the conventional RDP approach, as well as KT [9] and RFT [14]. Note again that the focusing method in [18] is equivalent to RFT in both performance and computational complexity and, hence, is represented by the RFT. Table III lists the default simulation parameters. We consider an LFMCW radar with a center frequency of 79 GHz. The bandwidth is 500 MHz, which corresponds to a range resolution of about 0.3 m. The PRI is 32 μs, with $V_{Ambi} = 213.6$ km/h. We choose the number of samples per chirp to be $N = 1024$. Thus, we have $\gamma = 488.3$ kHz. Unless specified otherwise, 1024 chirps, i.e., $L = 1024$ slow-time samples, are used for coherent processing, resulting in $T_{CPI} = 32$ ms. Unless specified otherwise, the linear interpolation and a factor of 4 zero-padding for slow-time FFT are used for the DRP algorithm, and Taylor windows with -50-dB sidelobe levels are used for both range and Doppler FFTs.

We first investigate the point spreading functions (PSFs) of the proposed DRP algorithm, as well as RDP, KF, and RFT, in Fig. 4. A point target is simulated at a range of 200 m with the relative radial velocity of 250 km/h moving toward to the radar. Therefore, within the CPI of 32 ms, the range migrates 2.2 m, i.e., around seven range bins. For comparison purposes, we provide the PSF of a stationary target in Fig. 4(a), formed by RDP. Fig. 4(b)–(e) shows the PSFs of the high-speed moving target, formed by RDP, KT, RFT, and DRP, respectively. Note that in Fig. 4(b) and (c), the true target velocity, i.e., -250 km/h, is folded to -36.4 km/h for RDP and KT, due to the velocity ambiguity caused by the PRI being too large. Comparing Fig. 4(a) and (b), we can see that the conventional RDP method suffers from the range- and Doppler-smearing problems with severely degraded range and velocity resolutions. From Fig. 4(c), we note that KT yields slightly better PSF than its RDP counterpart. However, it fails to completely mitigate the range migration problem due to the small PRF relative to the target Doppler shift, resulting in degraded range and Doppler resolutions. In contrast, as shown in Fig. 4(d) and (e), the RFT and DRP provide PSFs for the fast-moving target that are almost the same as that in Fig. 4(a) for the stationary counterpart. In other words, both RFT and DRP work well for the high-speed target with little performance degradations.

We now investigate the velocity ambiguity mitigation capability of the proposed DRP algorithm, as well as RFT, in the presence of multiple targets. The same radar parameters as given in Table III are used herein. Three moving targets are simulated at distances of 200, 203, and 195 m and with relative radial velocities -250, 50, and -150 km/h, respectively. Fig. 5(a)–(d) shows the range–velocity images, formed by RDP, KT, RFT, and DRP, respectively. The solid blue circles represent the true (range, velocity) locations of targets, while the dashed ones indicate the folded locations due to the ambiguities caused by the small PRF. As shown in Fig. 5(a) and (b), in this example, we have $V_{Ambi} = 213.6$ km/h and, hence, the unambiguous velocity interval of $[-106.8, 106.8)$ km/h for RDP and KT. In other words, RDP and KT cannot identify the true velocity for Target 1 among the two possibilities of -250 and -36.4 km/h, and for Target 3 among the two possibilities of -150 and
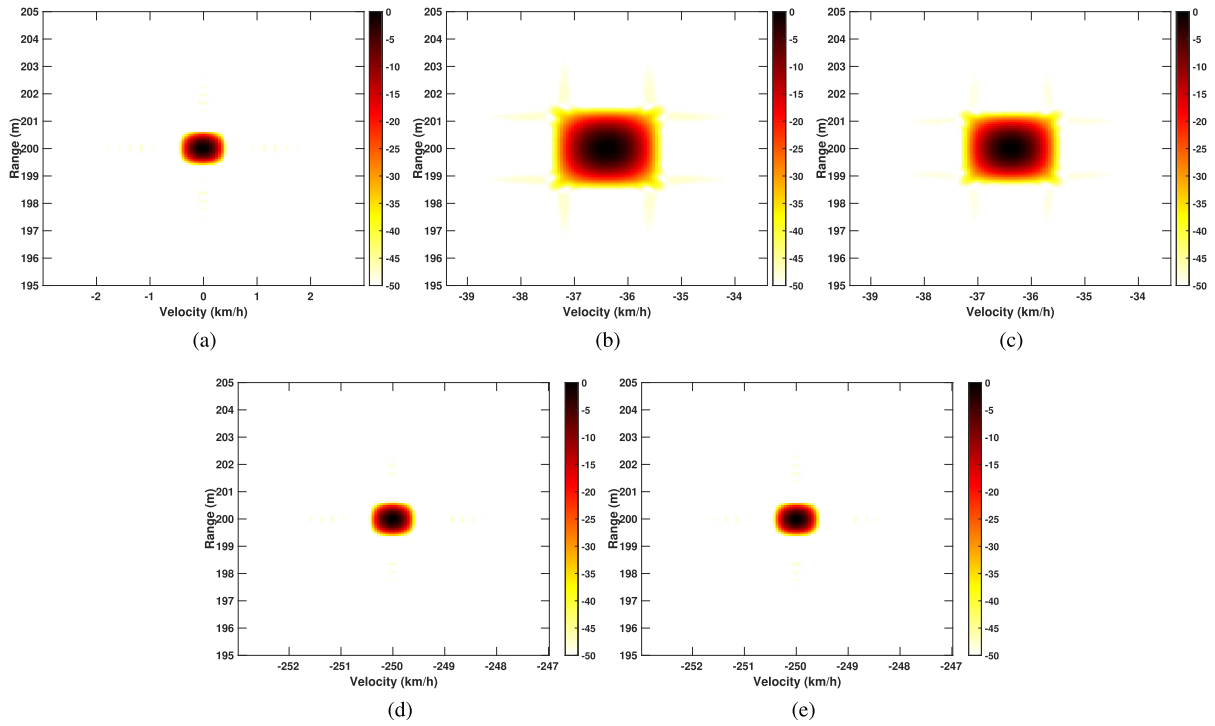
Fig. 4. Point spreading functions. (a) Stationary target: RDP. (b) Moving target: RDP. (c) Moving target: KT. (d) Moving target: RFT. (e) Moving target: DRP.
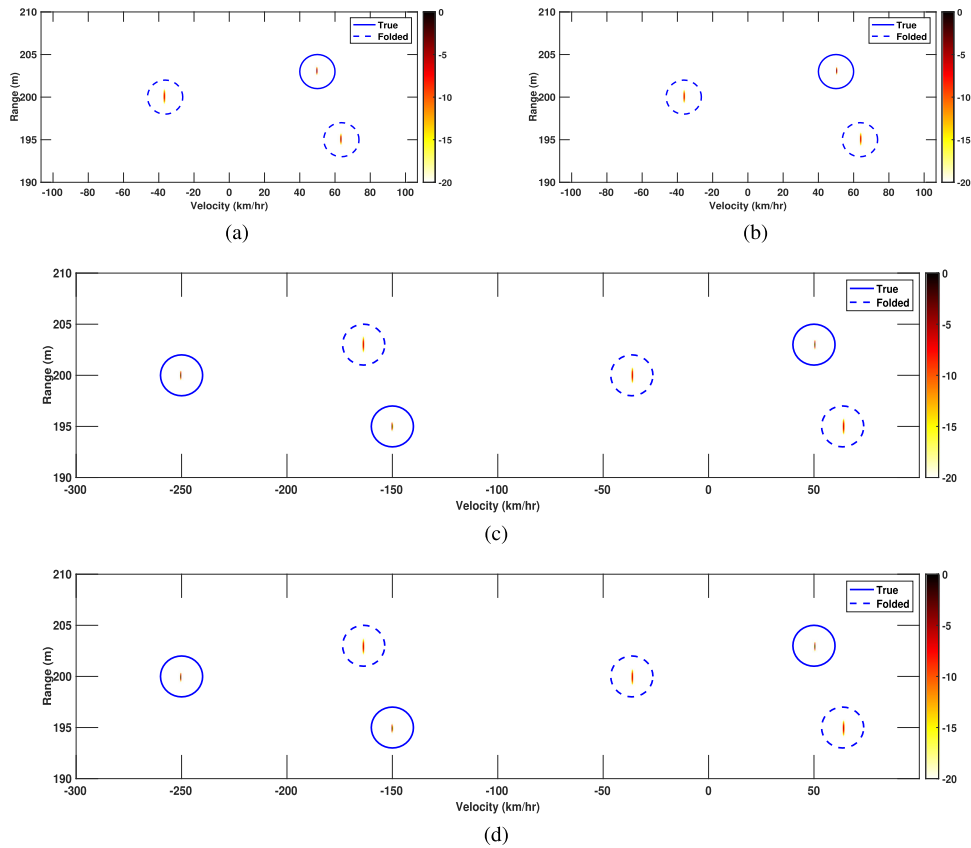

Fig. 5. Multitarget range–velocity imaging. (a) RDP. (b) RDP. (c) RFT. (d) DRP.
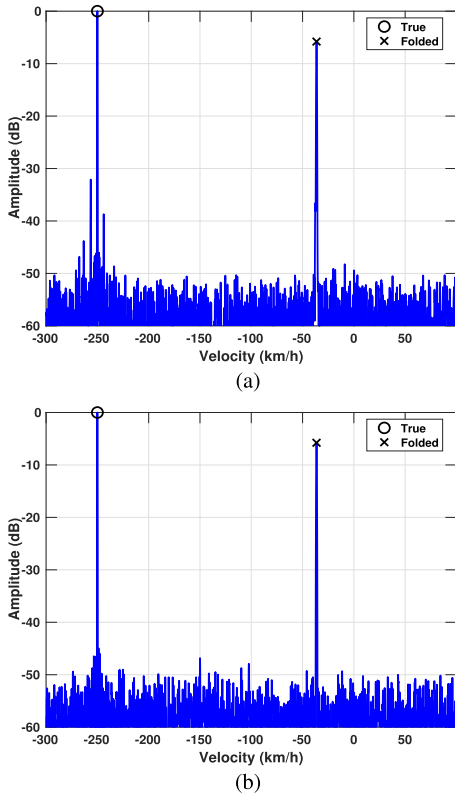
(a)

(b)

Fig. 6.   Velocity profiles formed by (a) RFT and (b) DRP.

Fig. 7.   Computational complexities of various algorithms.

64.6 km/h. Fig. 5(c) and (d) shows the range–velocity images, formed by RFT and DRP, with the velocity varying from −300 to 100 km/h. As we can see, both algorithms provide slightly tighter PSFs at the true velocities than their folded counterparts.

Consider Target 1, for example. Fig. 6(a) and (b) shows the target velocity profiles of Target 1, i.e., the horizontal slices of Fig. 5(c) and (d) at 200 m, formed by the RFT and DRP, respectively. In both figures, we can see a strong false peak at −36.4 km/h, which is the shadow of the true target at −250 km/h. This false peak is about 6 dB below the true peak at −250 km/h. Thus, the true target velocity can be identified by picking the stronger peak among the two possibilities.

We now investigate the computational complexities of various algorithms in Fig. 7. We fix the number of fast-time samples to be $N = 1024$ and vary the number of slow-time samples, i.e., L, from 16 to 4096. We assume that all algorithms use a factor of 4 zero-padding for both range and Doppler processing, and the RFT and DRP scan the radial velocities from −300 to 100 km/h. As we can see, KT and RDP have similar computational complexities. The proposed DRP algorithm is computationally slightly more intensive than its KT and RDP counterparts. This is mainly due to the wider velocity imaging size of DRP needed to mitigate the velocity ambiguities. Furthermore, DRP is computationally much more efficient than the RFT. For example, when $L = 1024$, DRP is two orders of magnitude more efficient than the RFT.
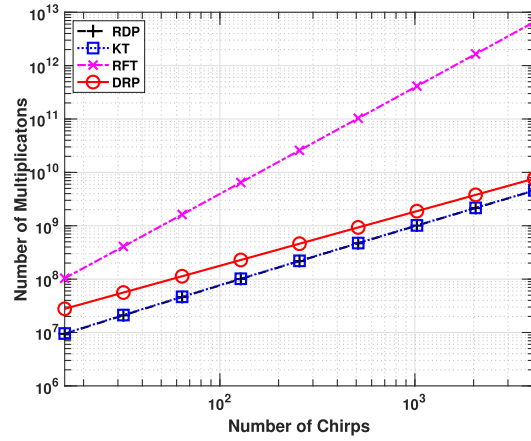
We next investigate the integration gains of various algorithms in Fig. 8. As shown above, the RFT, as well as the focusing method in [18], is equivalent to DRP in terms of performance, but is computationally much more intensive. Therefore, in Fig. 8, we only compare the coherent integration gains of the RDP and DRP algorithms. For comparison purposes, both theoretical and empirical numerical results, with and without the windowing techniques, are provided. Unless specified otherwise, the same simulation parameters as given in Table III are used herein, and a factor of 4 zero-padding is used for fast-time and slow-time FFTs for both algorithms.

In Fig. 8(a), we vary the number of chirps, i.e., the number of slow-time samples L, from 64 to 4096, with the corresponding CPI varying from 2 to 131 ms. First, note that the theoretical analysis and empirical results match each other well for both methods. As expected, the windowed DRP algorithm yields an approximate 3-dB performance loss than its nonwindowed counterpart. In both windowed and nonwindowed cases, the coherent integration gain of the proposed DRP algorithm increases monotonically as the CPI increases. The coherent integration gain increases 3 dB per doubling of the CPI. In contrast, the conventional RDP method suffers from the severe range/Doppler migration problems. The integration gain of DRP decreases drastically for a large CPI. The windowed RDP allows for a larger CPI than its nonwindowed counterpart, due to the reduced effective bandwidth and CPI caused by the windows. As theoretically analyzed in Section III-B, when the range/Doppler migration problems occur, the conventional RDP method suffers from a 3-dB loss per doubling of the CPI. The proposed DRP algorithm outperforms RDP significantly, especially for a large CPI. In the windowed case, it achieves approximately a 7-dB performance improvement over its RDP counterpart for $T_{CPI} = 32$ ms and 12-dB improvement for $T_{CPI} = 64$ ms.

Fig. 8(b) shows the coherent integration gain as a function of the radar bandwidth. We vary the radar bandwidth from 10 MHz to 2 GHz via increasing the chirp rate, i.e., γ. As we can see, in the low bandwidth case, the
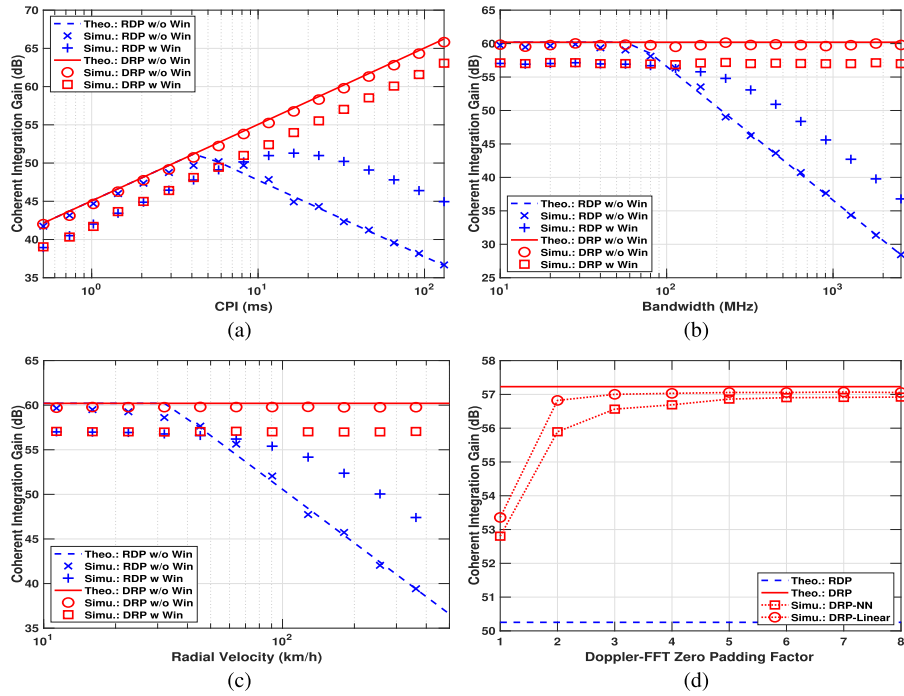
Fig. 8. Coherent integration gains as functions of (a) CPI, (b) bandwidth, (c) target radial velocity, and (d) FFT zero-padding factor for Doppler processing.

two methods provide similar coherent integration gains. However, when the radar bandwidth is larger than 50 or 100 MHz, the coherent integration gain obtained by the nonwindowed or windowed RDP method begins to decrease. For the high bandwidth case, the RDP coherent integration gain decreases 6 dB per doubling of the radar bandwidth, which is consistent with the theoretical analysis given in Section III-B. In contrast, the proposed DRP algorithm retains the same coherent integration gain for various radar bandwidths. The windowed DRP method outperforms its RDP counterpart by about 12 dB for the case of 1-GHz radar bandwidth. The performance improvement increases to 18 dB for the case of 2-GHz radar bandwidth.

In Fig. 8(c), we investigate the robustness of the methods against the target's radial velocity. As shown in Fig. 8(c), the proposed DRP algorithm attains the same integration gain for various target velocities. However, the conventional RDP method degrades dramatically as the target velocity increases. Consistent with the theoretical analysis given in Section III-B, for the high-speed scenario, the coherent integration gain of RDP decreases by about 6 dB per doubling of the target velocity. The windowed DRP algorithm achieves an improvement of about 7 dB over its RDP counterpart when the target relative radial velocity is $v = 250$ km/h.

We next consider the practical implementation of the proposed DRP algorithm in Fig. 8(d). Two interpolation methods, i.e., NN and linear interpolation, are investigated. We vary the FFT zero-padding factor from 1 to 8 for slow-time Doppler processing, i.e., with the
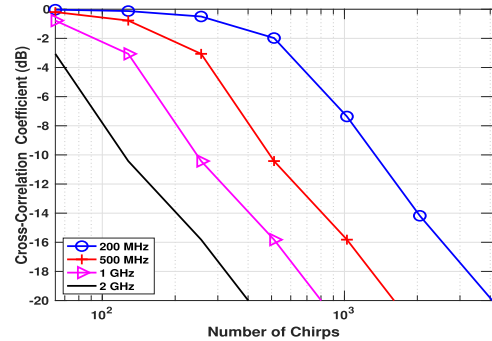
corresponding FFT size varying from 1024 to 8192. The theoretical performances of RDP and DRP are also provided for comparison purposes. As shown in Fig. 8(d), the performance of the linear interpolation method matches that of the theoretical analysis of DRP closely, with a factor of 2 zero-padding for the FFT. For NN, a factor of 4 zero-padding is needed to achieve a performance degradation of less than 0.5 dB.

Fig. 9 shows the cross-correlation coefficients of the reflected signals of two moving targets at the same range with the same folded velocities, as functions of the number of chirps L for various radar bandwidths B. We consider $k = 1$ in (18). As expected, the cross-correlation coefficient is reduced with an increased radar bandwidth or number of slow-time samples. Lower cross-correlation coefficients

Fig. 9. Cross-correlation coefficients of two moving targets' returns versus the number of slow-time samples for various radar bandwidths.

result in reduced shadow peaks relative to the true peak, making it easier for DRP to resolve the velocity ambiguity problems.

VI. CONCLUSION

In this article, we have investigated the range/Doppler migration and velocity ambiguity problems of high-speed moving target imaging using the LFMCW automotive radar. We have shown theoretically that in the presence range/Doppler migrations, the coherent integration gain of the conventional RDP method decreases 3 dB per doubling of the CPI and 6 dB per doubling of the radar bandwidth or target radial velocity. We have then introduced the DRP algorithm for high-speed moving target imaging using the LFMCW automotive radar. DRP can be used to mitigate the range/Doppler migrations and resolve the velocity ambiguity problem of high-speed moving target imaging. We have shown theoretically that DRP can achieve full coherent integration gains, as well as full range and full velocity resolutions, while maintaining a comparable computational complexity to that of the conventional RDP approach. The velocity ambiguity resolving capability of DRP, as a function of the number of chirps within a CPI or the radar bandwidth, has been analyzed theoretically. Finally, we have demonstrated the effectiveness and computational efficiency of the proposed DRP algorithm using several numerical examples.

APPENDIX A
PROOF OF (9)

For simplicity, we consider rectangular windowing. From (3), the RDP integration gain can be rewritten as

$$g_{RDP} = \frac{\left| \sum_l \sum_n e^{-j4\pi \frac{n l v \gamma T_{PRI}}{c}} \right|^2}{NL} = \frac{|h|^2}{NL} \qquad (20)$$

where

$$h = \sum_{l=-\frac{L}{2}}^{\frac{L}{2}} \sum_{n=-\frac{N}{2}}^{\frac{N}{2}} e^{-j4\pi \frac{n l v T_{PRI} \gamma}{c}}. \qquad (21)$$

Let $y_1 = \frac{l}{N}$ and $y_2 = \frac{n}{L}$, and

$$\mathcal{Y}_1 = \left\{ -0.5 \ -0.5 + \frac{1}{N}, \ \ldots, \ 0.5 - \frac{1}{N} \right\} \qquad (22)$$

$$\mathcal{Y}_2 = \left\{ -0.5, \ -0.5 + \frac{1}{L}, \ \ldots, \ 0.5 - \frac{1}{L} \right\}. \qquad (23)$$

Then, (21) can be rewritten as

$$h = \sum_{l \in \mathcal{Y}_1} \sum_{n \in \mathcal{Y}_2} e^{-j4\pi \frac{LN v \gamma T_{PRI}}{c} y_1 y_2}$$

$$= \sum_{l \in \mathcal{Y}_1} \sum_{n \in \mathcal{Y}_2} e^{-j2\pi \alpha y_1 y_2} \qquad (24)$$

with α defined in (8). Therefore, (21) can be approximated by the following integration formula:

$$h \approx LN \int_{-0.5}^{0.5} \int_{-0.5}^{0.5} e^{-j2\pi \alpha y_1 y_2} dy_1 dy_2. \qquad (25)$$

We can readily verify that the function $g(y_1, y_2) = y_1 y_2$ has a unique stationary point at $y_1 = y_2 = 0$ with the related Hessian matrix being a 2×2 antidiagonal identity matrix. By using the stationary phase approximation theorem [26], for a large $|\alpha|$, (25) can be approximated as follows:

$$h \approx \frac{LN}{|\alpha|} \qquad (26)$$

from which (9) is readily obtained.

APPENDIX B
RANGE AND DOPPLER RESOLUTIONS OF DRP

Again, for simplicity, we consider rectangular windowing, i.e., $w_D[l] = w_R[n] = 1$. The range profile represents the impact of a target located at the range–velocity cell (r_0, v) on $(r_0 + \delta^r, v)$ in the range versus velocity image, as a function of δ^r with δ^r representing the range offset from the true target location in range. From (3) and (10), we readily have

$$X_R(\delta^r) = L \sum_{n=-\frac{N}{2}}^{\frac{N}{2}-1} e^{j4\pi \frac{n \delta^r \xi}{c}} \propto \frac{\sin \left(\pi \frac{\delta^r}{\Delta_R} \right)}{\sin \left(\pi \frac{\delta^r}{N \Delta_R} \right)} \qquad (27)$$

with $\Delta_R = \frac{c}{2B}$ being the theoretical range resolution of the conventional RDP method for a stationary target. As we can see, (27), which is obtained via DRP for a moving target with any radial velocity, is identical to the range profile of RDP for a stationary target. Thus, the full range resolution $\frac{c}{2B}$ is achieved by DRP for a target with any radial velocity.

Similarly, the radial velocity profile represents the impact of a target located at range–velocity cell (r_0, v) on $(r_0, v + \delta^v)$ in the range versus velocity image, as a function of δ^v, with δ^v denoting the velocity offset from the true target velocity. Again, we have

$$X_V(\delta^v) = \sum_{l=-\frac{L}{2}}^{\frac{L}{2}-1} e^{j4\pi \frac{l \delta^v f_0 T_{PRI}}{c}} \left[\sum_{n=-\frac{N}{2}}^{\frac{N}{2}-1} e^{j4\pi \frac{n l \delta^v \xi T_{PRI}}{c}} \right]. \qquad (28)$$

Generally, the velocity profile in (28), which is obtained via DRP for a target with any radial velocity, is not the same as its RDP counterpart for a stationary target. However, when δ^v is small, e.g., when $\delta^v \leq \Delta_V = \frac{c}{2 f_0 T_{CPI}}$, we have

$$4\pi \frac{n l \delta^v \xi T_{PRI}}{c} \leq \pi \frac{NL \delta^v \xi T_{PRI}}{c} \leq \frac{\pi}{2} \frac{B}{f_0} \approx 0. \qquad (29)$$

Thus, for $\delta^v \leq \Delta_V$, we have

$$X_V(\delta^v) \approx N \sum_{l=-\frac{L}{2}}^{\frac{L}{2}-1} e^{j4\pi \frac{f_0 l \delta^v T_{PRI}}{c}} \propto \frac{\sin \left(\pi \frac{\delta^v}{\Delta_V} \right)}{\sin \left(\pi \frac{\delta^v}{L \Delta_V} \right)}. \qquad (30)$$

Therefore, the DRP velocity profile for a target with any radial velocity has a main-lobe shape similar to its RDP counterpart for a stationary target. Hence, we conclude that DRP can achieve the full velocity resolution for a target with any radial velocity.

APPENDIX C
PROOF OF (18)

Using the same technique as that used in Appendix A, (18) can be approximated by the following integration formula:

$$\rho \approx \int_{-0.5}^{0.5} \int_{-0.5}^{0.5} e^{-j2\pi \frac{LNk\gamma}{f_0} y_1 y_2} dy_1 dy_2. \tag{31}$$

Applying the stationary phase approximation theorem to (31) yields (19).

REFERENCES

[1] E. Yurtsever, J. Lambert, A. Carballo, and K. Takeda
     A survey of autonomous driving: Common practices and emerging technologies
     IEEE Access, vol. 8, pp. 58443–58469, 2020.

[2] D. Geronimo, A. M. Lopez, A. D. Sappa, and T. Graf
     Survey of pedestrian detection for advanced driver assistance systems
     IEEE Trans. Pattern Anal. Mach. Intell., vol. 32, no. 7, pp. 1239–1258, Jul. 2010.

[3] S. Saponara, M. S. Greco, and F. Gini
     Radar-on-chip/in-package in autonomous driving vehicles and intelligent transport systems: Opportunities and challenges
     IEEE Signal Process. Mag., vol. 36, no. 5, pp. 71–84, Sep. 2019.

[4] S. Sun, A. P. Petropulu, and H. V. Poor
     MIMO radar for advanced driver-assistance systems and autonomous driving: Advantages and challenges
     IEEE Signal Process. Mag., vol. 37, no. 4, pp. 98–117, Jul. 2020.

[5] A. G. Stove
     Linear FMCW radar techniques
     Proc. Inst. Elect. Eng. F, vol. 129, pp. 343–350, Oct. 1992.

[6] M. Richards
     Fundamentals of Radar Signal Processing. New York, NY, USA: McGraw-Hill, 2005.

[7] S. Brisken, F. Ruf, and F. Hohne
     The recent evolution of automotive imaging radar and its information content
     IET Radar, Sonar Navigation, vol. 12, Apr. 2018, doi: 10.1049/iet-rsn.2018.0026.

[8] B. Carlson, E. Evans, and S. Wilson
     Search radar detection and track with the Hough transform. I. System concept
     IEEE Trans. Aerosp. Electron. Syst., vol. 30, no. 1, pp. 102–108, Jan. 1994.

[9] R. P. Perry, R. C. DiPietro, and R. L. Fante
     SAR imaging of moving targets
     IEEE Trans. Aerosp. Electron. Syst., vol. 35, no. 1, pp. 188–200, Jan. 1999.

[10] D. Cerutti-Maori, J. Klare, A. R. Brenner, and J. H. G. Ender
     Wide-area traffic monitoring with the SAR/GMTI system PAMIR
     IEEE Trans. Geosci. Remote Sens., vol. 46, no. 10, pp. 3019–3030, Oct. 2008.

[11] D. Vu, B. Guo, L. Xu, and J. Li
     SAR based adaptive GMTI
     Proc. SPIE, vol. 7699, Apr. 2010, Art. no. 76990H.

[12] S.-S. Zhang, T.T. Z.Long, and H.-P. Yuan
     Dim target detection based on keystone transform
     In *Proc. IEEE Int. Radar Conf.*, 2005, pp. 889–894.

[13] Y. Li, T. Zeng, T. Long, and Z. Wang
     Range migration compensation and Doppler ambiguity resolution by keystone transform
     in *Proc. CIE Int. Conf. Radar*, 2006, pp. 1–4.

[14] J. Xu, J. Yu, Y. Peng, and X. Xia
     Radon-Fourier transform for radar target detection, I: Generalized Doppler filter bank
     IEEE Trans. Aerosp. Electron. Syst., vol. 47, no. 2, pp. 1186–1202, Apr. 2011.

[15] J. Xu, J. Yu, Y. Peng, and X. Xia
     Radon-Fourier transform for radar target detection, II: Blind speed sidelobe suppression
     IEEE Trans. Aerosp. Electron. Syst., vol. 47, no. 4, pp. 2473–2489, Oct. 2011.

[16] J. Yu, J. Xu, Y. Peng, and X. Xia
     Radon-Fourier transform for radar target detection, III: Optimality and fast implementations
     IEEE Trans. Aerosp. Electron. Syst., vol. 48, no. 2, pp. 991–1004, Apr. 2012.

[17] O. Longman and I. Bilik
     Spectral Radon-Fourier transform for automotive radar applications
     IEEE Trans. Aerosp. Electron. Syst., vol. 57, no. 2, pp. 1046–1056, Apr. 2021.

[18] F. Uysal and N. Goodman
     The effect of moving target on range-Doppler map and back-projection algorithm for focusing
     In *Proc. IEEE Radar Conf.*, Philadelphia, PA, USA, 2016, pp. 1–5.

[19] F. Uysal
     Comparison of range migration correction algorithms for range-Doppler processing
     J. Appl. Remote Sens., vol. 11, no. 3, pp. 1–10, 2017.

[20] J. Vovnoboy, R. Levinger, N. Mazor, and D. Elad
     A dual-loop synthesizer with fast frequency modulation ability for 77/79 GHz FMCW automotive radar applications
     IEEE J. Solid-State Circuits, vol. 53, no. 5, pp. 1328–1337, May 2018.

[21] J. Y. N. Cho
     Multi-PRI signal processing for the terminal Doppler weather radar. Part II: Range-velocity ambiguity mitigation
     J. Atmos. Ocean. Technol., pp. 1507–1519, Oct. 2005.

[22] X. Xia and G. Wang
     Phase unwrapping and a robust Chinese remainder theorem
     IEEE Signal Process. Lett., vol. 14, no. 4, pp. 247–250, Apr. 2007.

[23] Y. Li, C. Liang, M. Lu, X. Hu, and Y. Wang
     Cascaded Kalman filter for target tracking in automotive radar
     J. Eng., vol. 2019, no. 19, pp. 6264–6267, 2019.

[24] I. Shapir, I. Bilik, and G. Barkan
     Doppler ambiguity resolving in TDMA automotive MIMO radar via digital multiple PRF
     In *Proc. IEEE Radar Conf.*, Oklahoma City, OK, USA, 2018, pp. 0 175–0180.

[25] F. G. Jansen
     Automotive radar Doppler division MIMO with velocity ambiguity resolving capabilities
     In *Proc. 16th Eur. Radar Conf.*, Paris, France, 2019, pp. 245–248.

[26] V. Guillemin and S. Sternberg
     Geometric Asymptotics. Providence, RI, USA: Amer. Math. Soc., 1990.

Luzhou Xu (Senior Member, IEEE) received the B.Eng. and M.S. degrees in electrical engineering from Zhejiang University, Hangzhou, China, in 1996 and 1999, respectively, and the Ph.D. degree in electrical and computer engineering from University of Florida, Gainesville, FL, USA, in 2006.

He is currently a Research Engineer with the Advanced Technology and Projects Group, Google, Mountain View, CA, USA. Prior to this, he has been with ZTE, Philips Research, ArrayComm, IAA, University of Florida, FutureWei Technologies, and Amazon. He has authored/coauthored more than 70 peer-reviewed papers. His research interests include signal processing, machine learning, and their applications.

Jaime Lien received the bachelor's and Master's degrees in electrical engineering from the Massachusetts Institute of Technology, Cambridge, MA, USA, and the Ph.D. degree in electrical engineering from Stanford University, Stanford, CA, USA, where her research focused on interferometric synthetic aperture radar theory and techniques.

She is currently the Radar Research Lead of Project Soli with the Advanced Technology and Projects Group, Google, Mountain View, CA. She leads a technical team developing novel radar sensing techniques and systems for human perception and interaction. Soli radar technology has enabled new modes of touchless interaction in consumer wearables and devices, including Google's Pixel 4 and the Nest Thermostat. Prior to Google, she worked as a Communications Engineer with NASA's Jet Propulsion Laboratory. Her current research interests include radar signal processing and sensing algorithms, modeling and analysis of the underlying radio frequency physics, and inference on radar data.

Jian Li (Fellow, IEEE) Author photograph and biography not available at the time of publication.